A Full-Area Passivating Hole Contact in Silicon Solar Cells Enabled by a TiO_x/Metal Bilayer

Takuya Matsui,[*†] *Shona McNab,*[‡] *Ruy Sebastian Bonilla,*[‡] *Hitoshi Sai* [†]

[†]Global Zero Emission Research Center, National Institute of Advanced Industrial Science and Technology (AIST), 1-1-1 Umezono, Tsukuba, Ibaraki, 305-8568, Japan

[‡] Department of Materials, University of Oxford, Parks Rd, Oxford, OX1 3PH, United Kingdom

KEYWORDS

titanium oxide, atomic layer deposition, passivating contact, silicon, solar cell, hole transport, work function, metallization

ABSTRACT

Passivating contacts, featuring dual function of defect passivation at the semiconductor surface and extracting one type of charge carrier, are recognized as the key enabler in achieving high-efficiency Si solar cells. In particular, a dopant-free and full-area passivating hole contact is critical to replace the conventional rear structure that features a partial Si-metal contact design with insulator interlayers. Herein, titanium oxide (TiO_x) nanolayers (~5 nm) grown by atomic layer deposition over the full area of Si surface followed by metal capping such as Ag are shown to provide efficient passivation and hole extraction with high optical reflectivity at the rear of Si solar cells. The proof-of-concept solar cells with either *p*- or *n*-Si absorber demonstrate ~20% efficiency exhibiting higher infrared response compared with the conventional rear structure. Photoluminescence and electrical measurements on different TiO_x/metal bilayers revealed that the field-effect passivation mechanism plays a major role in device performance, exploiting the high-concentration negative charge (>10^{12} q cm^{-2}) at the Si/TiO_x interface and the high work function (~>4.6 eV) of the capping metal. The developed contact offers great potential for boosting the efficiency and simplifying manufacturing of commercial Si solar cells.

1. Introduction

Photovoltaic power is recognized as one of the major renewable energies and a key enabler for the energy transition towards carbon neutral society. Currently, photovoltaic panels based on crystalline Si solar cells account for ~95% of the global solar generation market share (1), and this situation is expected to continue in the next few decades. The mainstream technology today is

known as the passivated emitter and rear cell (PERC) (2,3) architecture. It features passivation of the rear surface of a *p*-type Si (*p*-Si) absorber by dielectric layers such as Al_2O_3 and SiN_x. Due to their electrically insulating characteristics, local metallization via contact holes through the dielectric layers is necessary to collect photogenerated carriers (holes) from the *p*-Si absorber to the rear electrode. Although PERC is an established technology, the device performance is essentially limited by the charge carrier recombination at the metallized area where the surface defects remain electrically active. Such an unpassivated area of Si is responsible for the relatively low open-circuit voltage (V_{oc}) in PERC solar cells. Thus, a functional interlayer material called "passivating contact" is highly desirable to enable efficient passivation and hole extraction simultaneously (4). So far, Si-based passivating contacts, such as hydrogenated amorphous Si (a-Si:H) (5-7) and ultrathin SiO_2/polycrystalline Si (SiO_2/poly-Si) (8,9) have been successfully implemented to demonstrate conversion efficiencies above 25%. The drawbacks of these Si-based passivating contacts are the use of relatively costly deposition tools for thin-film Si deposition, the sensitivity of a-Si:H to moderate temperatures, and the lack of a highly passivating and hole-selective SiO_2/poly-Si contact. In fact, the SiO_2/poly-Si contacts have been mostly applied as an electron-selective passivating contact.

Recently, non-Si hole contact materials are emerged featuring high-work function metal oxides, e.g., MoO_x (10,11), WO_x (11,12) and V_2O_x (12,13), and organic materials such as PEDOT:PSS (14). A 23.5% efficient cell has been demonstrated using a MoO_x hole contact (15). However, due to its relatively poor passivation capability, a buffer layer such as an intrinsic a-Si:H layer is still necessary prior to the deposition of the metal oxide layer, which is less attractive from an industrial perspective. Recently, we have developed a titanium oxide (TiO_x) nanolayer grown by atomic layer deposition (ALD) that uniquely acts as a hole-selective passivating contact in Si

solar cells (16,17), which is opposite from the previous understanding that TiO_x is an electron selective material with respect to various solar cell absorbers including Si (18,19), III-V (20) and perovskite (21,22). Using our TiO_x as a front hole contact, 21.1% efficiency has been demonstrated without using any buffer layer (17). Although the light-induced degradation caused by the UV illumination remains a challenge to overcome, such degradation is not present if the TiO_x is applied to the unilluminated rear surface. This is particularly interesting for its application to PERC Si solar cells.

In this paper we apply our hole selective TiO_x nanolayer to the rear surface of Si solar cells in order to exploit its potential for a full area rear contact instead of the conventional partially contacted scheme. We demonstrate proof-of-concept *p*- and *n*-Si solar cells exhibiting efficiency of ~20%, and compare them with the benchmarking Si heterojunction (SHJ) hole contact (*i*-*p* a-Si:H layers stack) in terms of passivation, hole selectivity and optical reflection. We show the importance of the work function of the capping metal layer deposited on top of the TiO_x layer to make it an efficient hole-selective passivating contact. The mechanism behind the unique feature of our TiO_x contact is discussed based on various characterization results.

2. Results and discussion

Device structures fabricated in this study using *p*- and *n*-Si absorbers are schematically depicted in Figures 1a and 1b, respectively. All the solar cells have textured surface on the front side while the rear surface remains planar. As a hole contact, TiO_x layer with a thickness of ~5 nm was deposited on the rear surface of Si by thermal ALD, and it was subsequently treated with a hydrogen plasma (17). Then, the TiO_x layer was capped with a metal over the entire area. To investigate the impact of capping metal on the device performance, we deposited various metal

thin layers with a thickness of ~50 nm followed by a thick Ag layer (~700 nm). The electron contact was formed on the front textured side using an *i*-*n* a-Si:H stack. On top of the *n* a-Si:H layer, an indium-tin oxide (ITO) layer and an Ag grid were deposited by sputtering. The layer stack configuration is the same regardless of *p*- or *n*-Si substrate. The cell area was defined by the electrode area of the emitter side. Namely, the ITO front electrode for *p*-Si and the metal rear electrode for *n*-Si. For current density-voltage (J-V) measurements, a black shading mask was used to define the illumination area of 1.045 cm^2 which is smaller than the electrode area of the emitter (1.12 cm^2).

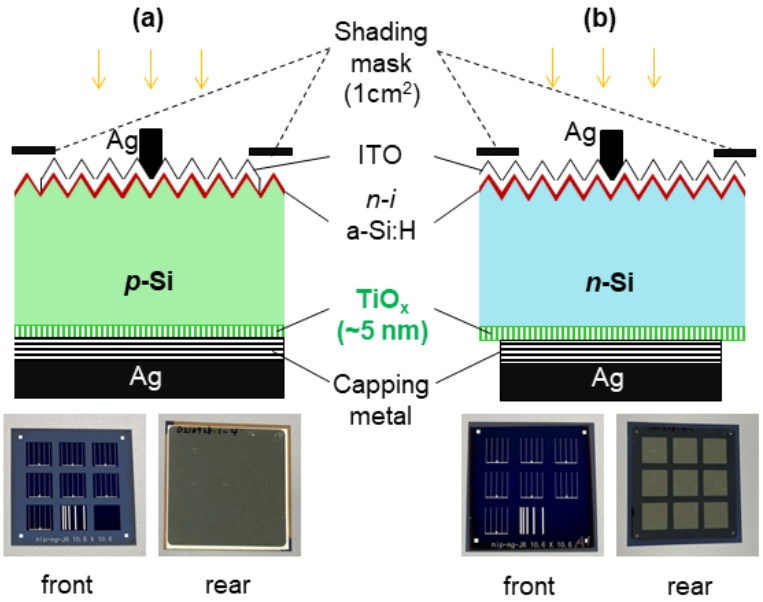

Figure 1. Schematic illustrations of (a) *p*-Si and (b) *n*-Si solar cells and the corresponding photos of solar cells in a Si substrate taken from the front (without shading mask) and the rear side. The electrode for the emitter side (front ITO for *p*-Si and rear metal for *n*-Si) was patterned to define the device area. The surface of Ag layers was coated with thin ITO layers (20 nm) for protection.

The impact of varying capping metal on the device performance is shown in Figure 2. Here we employed seven different metals: Al, Ti, Cu, Ag, Au, Ni and Pt, which were chosen to examine a range of work functions (WF) of metals. Due to the techniques available on the deposition systems, Cu and Ag were deposited by DC magnetron sputtering while the other metals were

deposited by electron-beam evaporation. We note that the influence of using different deposition methods is minor as will be discussed later. As shown in Figures 2a-d, the device performance does not depend much on the absorber polarity, whereas it is significantly influenced by the choice of capping metal deposited on top of the TiO_x layer. Higher short-circuit current density (J_{sc}) is obtained for Al, Cu, Ag and Au which are the typical metals exhibiting high optical reflectivity in the near infrared. By comparing the external quantum efficiency (EQE) spectra of solar cells, as shown in Figure 2e, it is evident that the J_{sc} is determined by the infrared response (>900 nm) of solar cells. This can be attributed to the reflectivity of the metals used, as the incident light for >900 nm is not fully absorbed by Si before reaching the rear contact and thus the optical reflection at the rear contact contributes greatly to enhancing the infrared response. The choice of Cu, Ag and Au results in almost the same J_{sc} and infrared response, as the reflectivity of these metals exceeds 95% for >900 nm (23). On the other hand, we find that the WF of the capping metal plays a decisive role in the V_{oc} which is a measure of both the passivation capability and the hole selectivity (24). Here, WF values were obtained from Ref. (25) with the exception of Ag for which the reported WF of ~4.2 eV is too low to explain the tendency. In fact, it deviates substantially in various reports and depends on the crystallographic orientation (26,27) and the oxygen adsorption (28)/incorporation (29). If we took the WF of Ag as ~4.7 eV from Ref. (28-30), a critical WF is found at 4.3-4.6 eV below which an abrupt decrease in V_{oc} occurs. On the other hand, relatively high V_{oc} can be obtained regardless of the capping metal if WF> 4.6 eV. The fill factor (FF) is less dependent on the choice of the capping metal, except for Ti, Cu and Ag, which will be discussed below. Overall, the efficiency is predominantly determined by V_{oc}. The highest efficiency is obtained for Ag due to the superior FF among the capping metals investigated.

Figure 2f shows a cross-sectional high-angle annular dark field scanning transmission electron microscopy (HAADF-STEM) image of the *p*-Si solar cell with a TiO_x/Ag rear contact. The corresponding elemental maps and line scans analyzed by the energy-dispersive x-ray spectroscopy (EDX) are shown in Figures 2g and 2h. An abrupt TiO_x/Ag interface is identified without any detectable Ag penetration to the Si surface, indicating that the charge carrier transport takes place through the semiconducting TiO_x layer. A ~1.5 nm-thick spontaneous intermixing layer consisting of Ti, O and Si atoms is created at the Si/TiO_x interface similar to previous work (17). An enhanced hydrogen incorporation was observed in this intermixing layer particularly after hydrogen plasma treatment (HPT) and the subsequent annealing, by which the surface passivation and hole selectivity were effectively improved (17). The hole selectivity of our TiO_x has been also associated with the specific chemical composition in the intermixing layer (17). Here, we clarify that the capping metal plays an additional important role in this unique functionality of the TiO_x as a hole-selective passivating contact.

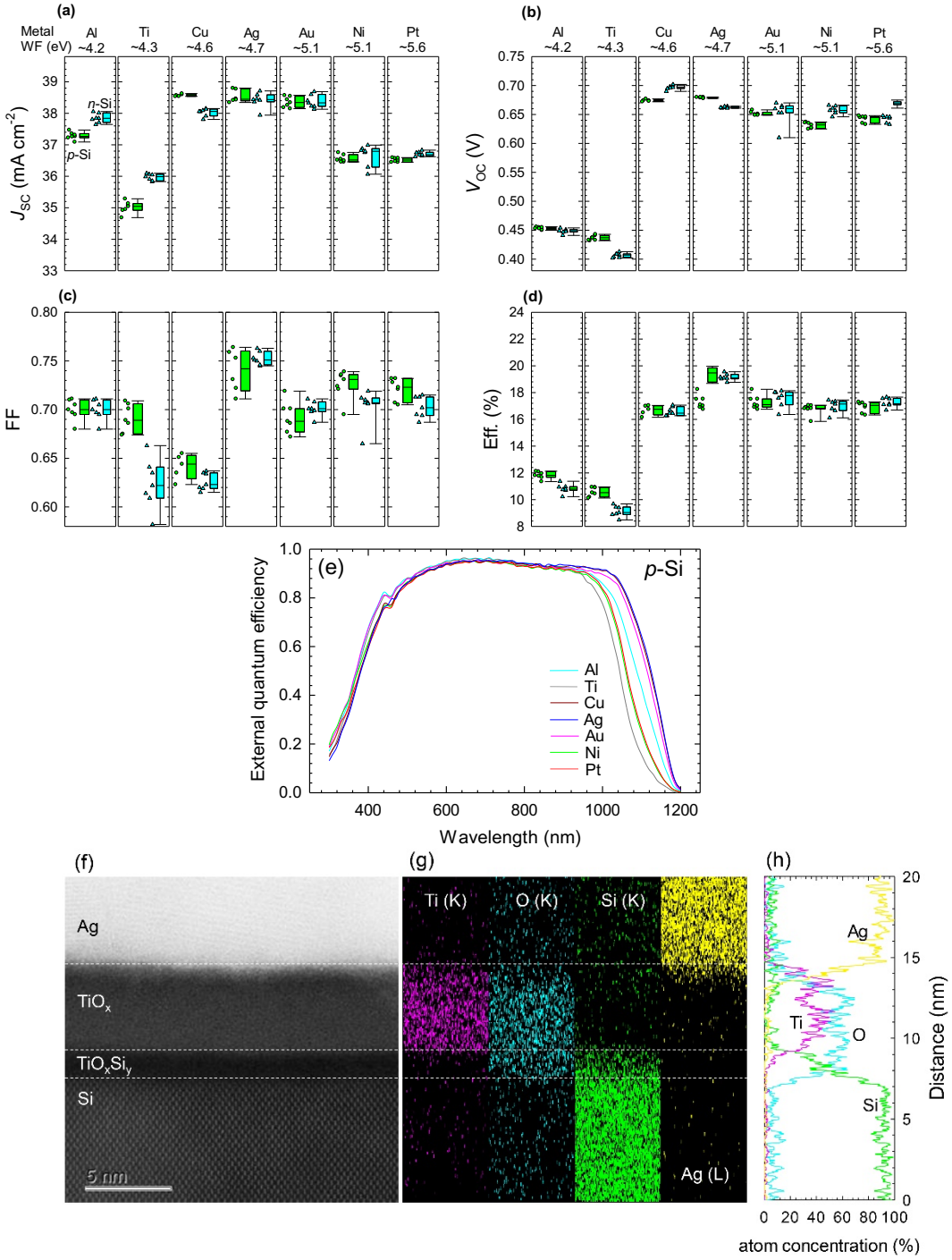

Figure 2. (a)-(d) J-V parameters of *p*-Si (green circles) and *n*-Si (cyan triangles) solar cells with various metals (Al, Ti, Cu, Ag, Au, Ni and Pt). The WF of Ag referred to Ref. (28-30) while those of the rest of metals referred to Ref (25). (e) EQE spectra of solar cells with different metals (Al, Ti, Cu, Ag, Au, Ni and Pt) on top of the TiO_x layer at the rear of *p*-Si solar cells. (f) HAADF-STEM cross-sectional image of *p*-Si solar cell that has a TiO_x/Ag rear contact. (g) EDX elemental maps and (h) line scans of Ti, O, Si and Ag. Note that the width of EDX maps was reduced to 25% for presentation.

To elucidate the origin of the dependence of V_{oc} on the WF of metal, we applied photoluminescence (PL) imaging to the working devices. High PL intensity originates from the radiative recombination of photogenerated electron-hole pairs in Si absorber, which decreases when the rate of the non-radiative recombination dominates via bulk or surface defects. In Figure 3, the PL image and its intensity strongly depend on what metal is deposited on top of the TiO_x layer. By using a quasi-steady-state photo-conductance (QSSPC) technique (31), we confirmed high effective minority carrier lifetime (τ_{eff} >2 ms for *p*-Si and >5 ms for *n*-Si at an injection level of 10^{15} cm^{-3}) and high implied open-circuit voltage (iV_{oc}>0.715 V for both *p*-Si and *n*-Si) for all samples prior to metal capping. Thus, the passivation of Si rear surface is altered by the capping metal. Almost no PL signal is observed for Al and Ti contacted cells, indicating that lifetime of excess photogenerated carrier is markedly lowered when applying low-WF (<4.3 eV) metals. In particular, by looking at the PL images for the *n*-Si solar cells for which the rear metal contacts are patterned, it is clear that the PL intensity is lowered only for the metallized area. This provides evidence that metal-induced degradation in the passivation occurs. By comparing these PL images with the J-V parameters shown in Figure 2, we conclude that V_{oc} is dominated by the level of rear surface passivation and it is significantly impacted by the WF of the capping metal. Meanwhile, brighter PL images can be seen for the solar cells with high-WF (>4.6 eV) metals. In particular, PL intensities for Ag, Cu and Au are higher than for Ni and Pt because the luminescent emission is enhanced by light reflection at the rear metal layer. A slightly lower PL intensity for Au than for Ag and Cu is possibly attributed to the different deposition method used (i.e., electron-beam evaporation for Au and sputtering for Ag and Cu). Although it is a minor effect in this study, the radiation damage in Si caused by heat and/or high-energy photons/reflected electrons during the electron-beam evaporation is a plausible explanation for the slightly lower V_{oc} for Au, Ni and Pt

than for Ag and Cu, as shown in Figure 2(b). Nevertheless, this effect is negligible when comparing the effect of WFs for Al and Au, as the electron-beam energy needed for Al evaporation is lower than for Au. It should be added that the Ag formation by other thermal evaporation method results in the similar passivation performance (*e.g.*, V_{oc}) with the cell by sputtered Ag. However, we find that FF depends slightly on metallization method (sputtering *vs*. evaporation) and condition (*e.g.*, sputtering power). The optimization of the metallization method and condition is a technical issue to be addressed for further improvement.

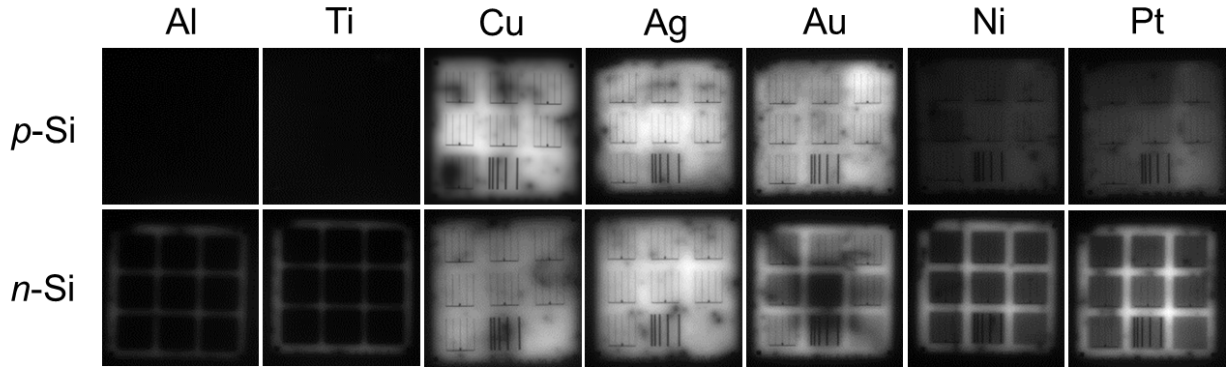

Figure 3. PL images of the *p*-Si (upper row) and *n*-Si (lower row) solar cells with different metals (Al, Ti, Cu, Ag, Au, Ni and Pt) deposited on top of the TiO_x layer at the rear of solar cells.

To gain insight into the mechanism behind TiO_x passivation and its dependence on the WF of the capping metal, we performed conductance-voltage (G-V) measurements on the *n*-Si/TiO_x/metal stack with thermally evaporated Al and Au. We chose G-V instead of capacitance-voltage measurement (16) since the conductive nature of the nanolayer dielectric prevented meaningful capacitances from being measured in this structure. This is expected when the metal-insulator-semiconductor is built to function as a highly conductive contact. Example capacitance measurements are included in Supporting Information Figure S1a. We complemented the G-V measurements by conducting Kelvin Probe measurements of contact potential difference (CPD) in

the *n*-Si/TiO_x structure prior to metal deposition. The resulting G-V characteristics are illustrated in Figure 4a. The level of conductance observed (>mS) originates both from interface states and charge carriers injected across the TiO_x layer. The conductance signal arising from interface states is due to the capture and emission of carriers at the surface, which is a function of the surface carrier concentration, and has typical values in the range of 1-100 μS. The large observed conductance is hence primarily given by the transport of charge carriers across the TiO_x rather than inter-band transitions, and thus it is not possible to apply Nicollian and Goetzerber method (32) to elucidate the concentration of interface states. Here instead we have modelled the interface carrier concentration as a function of (i) an assumed interface state density function and capture cross sections, (ii) a concentration of fixed interface charge (Q_f) inferred from CPD measurements of the *n*-Si/TiO_x interfaces, and (iii) the value of WF expected for each metal. For this we have followed the modelling procedure and adapted the parameters reported in Ref. (32-34). Figure 4a shows the presence of an onset of conductance across the TiO_x layer, labelled by the shadowed region, occurring for more positive voltages. In the dark, maximum conductance only occurs when the surface becomes electron rich since this is *n*-Si, which occurs under the positive applied voltage. We have therefore used the value of gate voltage at which the onset of conductivity occurs as an indication of the condition for flat band in the structure. Figure 4a bottom shows the absolute value of charge concentration at the surface, when fitted to the onset of conductivity chosen here at 2 mS. The fitting values of WF and Q_f used to model such curves are included in the plot. These calculations indicate that the TiO_x layer presents a large concentration of negative charge whether Al or Au are deposited as top contact, which is in agreement with our previous work (16). We have confirmed the presence of negative charge using CPD measurements in a Kelvin Probe instrument as presented in Figure 4b. CPD is a measure of the surface potential on the structure referred to

the local ground electrode in the instrument. Surface potential includes the effects of semiconductor doping, surface space charge regions, and any charge either at interfaces or on the surface of dielectric coatings (36). CPD can be measured both in the dark and under illumination, and the surface photovoltage calculated as the $CPD_{dark} - CPD_{light}$, which shows a positive value for the TiO_x samples in this work. Positive surface photovoltage was inherently observed in our TiO_x samples for all steps of the processing (Supporting Information: Figure S2). This indicates the presence of negative charge of at least 10^{12} q cm^{-2} inside the dielectric nanolayer, comparable to that observed in Si/Al_2O_3 (Supporting Information: Figure S1b) or super acid passivation schemes (37), and only possible for negatively charged dielectric films following the models reported in Ref. (36, 38-40). It is also evident that metals with larger WF such as Au produce a larger amount of hole accumulation at the surface, thus requiring a larger gate voltage to achieve the flat band regime in *n*-Si. For Au, flat band is achieved for gate voltages in the order of 0.9 V. In contrast, the flat band onset occurs at a gate voltage of 0.3 V for an equivalent sample with an Al metal contact. In absence of any applied voltage, such Al metal gate reduces the field effect mechanism provided by the negatively charged TiO_x, reducing the hole concentration and leading to higher recombination from the higher presence of electrons at the surface.

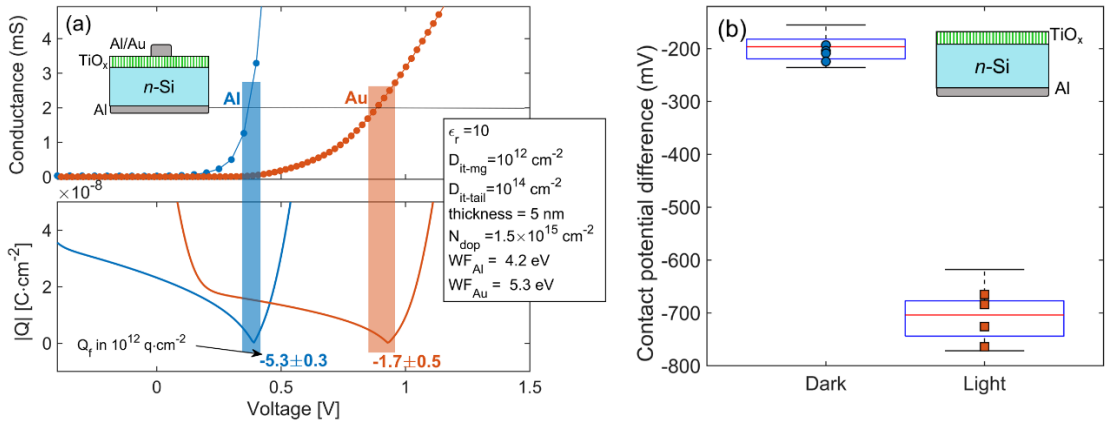

Figure 4. (a) Conductance-voltage measurements of metal-Si-TiO_x-Al and metal-Si-TiO_x-Au structures, using planar (100) 2 Ωcm *n*-Si, and including modelled dependence of the surface charge concentration as a function of the metal and internal dielectric-Si interface charge. (b) Contact potential difference measurements using Kelvin Probe, indicating a positive value of surface photovoltage (CPD_{dark}-CPD_{light}) in correspondence to a negatively charged dielectric nanolayer.

From the PL, G-V, and CPD measurements, we conclude that the field-effect passivation is a major mechanism at the Si/TiO_x interface due to the presence of the high concentration of negative fixed charge. Such negative fixed charge induces carrier accumulation or inversion at the Si/TiO_x interface for *p*-Si and *n*-Si, respectively. The presence of the fixed charge hence provided both functions of field-effect passivation and hole selectivity. From our experimental results, such carrier profile can be preserved if the WF of the capping metal is higher than >4.6 eV.

Next, we studied the device performance of *p*- and *n*-Si solar cells featuring TiO_x/Ag bilayer rear contact which showed the highest efficiency among the solar cells investigated. The results of the best performing *p*- and *n*-Si solar cells are summarized in Table 1. For comparison, the results of solar cells that have SHJ rear structure (i.e., *i*-*p* a-Si:H hole contact) with and without an ITO interlayer between *p* a-Si:H and Ag layers are included. Furthermore, those without any passivating hole contact at the rear (i.e., direct metallization on Si rear surface) are also included to exemplify the extreme recombination case. In both the *p*- and *n*-Si solar cells, the TiO_x/Ag contact shows as good performance as the conventional SHJ hole contact with an ITO interlayer. They outperform the SHJ hole contact that has no ITO interlayer, offering an opportunity for this new TiO_x/Ag contact to act as an ITO-free rear contact in SHJ solar cells (41). EQE spectra show the greater infrared response for TiO_x/Ag compared to the SHJ hole contact especially for that with an ITO interlayer, as shown in Figures 5a and 5b. This demonstrates that TiO_x/Ag bilayer provides a superior optical reflector compared to ITO/Ag. A slightly lower FF is found for *n*-Si than for *p*-

Si, regardless of the hole contact structure, and is attributed to our unoptimized rear junction device design. Meanwhile, the solar cell without a passivating hole contact results in very poor performance. In such devices, it is noteworthy that the solar cell performance reductions depend largely on the Si polarity, i.e., decreasing J_{sc} for *p*-Si but deceasing V_{oc} and FF for *n*-Si. EQE spectrum of the *p*-Si solar cell shows markedly low response for wavelengths >900 nm. As solar cell is a minority carrier device and the minority carriers generated in the absorber are collected by the emitter, the solar cell performance is influenced differently by the rear surface recombination depending on the emitter position (front or rear). In *p*-Si, minority carrier electrons are collected by the front emitter (*i*-*n* a-Si:H) in our device configuration. If the rear surface is strongly recombination active without a back surface field, the rear surface recombination prevents electrons from diffusing towards the front emitter, explaining the decrease in the long wavelength response. In *n*-Si, on the other hand, minority carrier holes are collected by the rear emitter (TiO_x) in our device configuration. Even if the rear surface is unpassivated, the rear surface recombination does not inhibit hole diffusion towards the rear emitter. Thus, J_{sc} and the long wavelength response are not decreased much. However, due to the lack of the induced junction formation (band bending) in *n*-Si, V_{oc} and FF are markedly low. These results manifest the important role of well-designed carrier-selective passivating contacts in maximizing Si solar cell performance.

Table 1. J-V parameters of *p*-Si and *n*-Si solar cells with different hole contact structures.

Absorber	Hole contact	Capping layer	Device #	J_{sc} (mA cm^{-2})	V_{oc} (mV)	FF	Eff. (%)
***p*-Si**	**TiO_x**	**Ag**	**A**	**38.4**	**686**	**0.772**	**20.3**
	a-Si:H *i-p*	ITO/Ag	B	38.4	697	0.772	20.7
	a-Si:H *i-p*	Ag	C	38.2	683	0.740	19.3
	-	Ag	D	35.3	574	0.791	16.0
***n*-Si**	**TiO_x**	**Ag**	**E**	**38.4**	**693**	**0.722**	**19.2**
	a-Si:H *i-p*	ITO/Ag	F	37.7	708	0.742	19.8
	a-Si:H *i-p*	Ag	G	37.9	694	0.716	18.8
	-	Ag	H	37.0	127	0.427	2.0

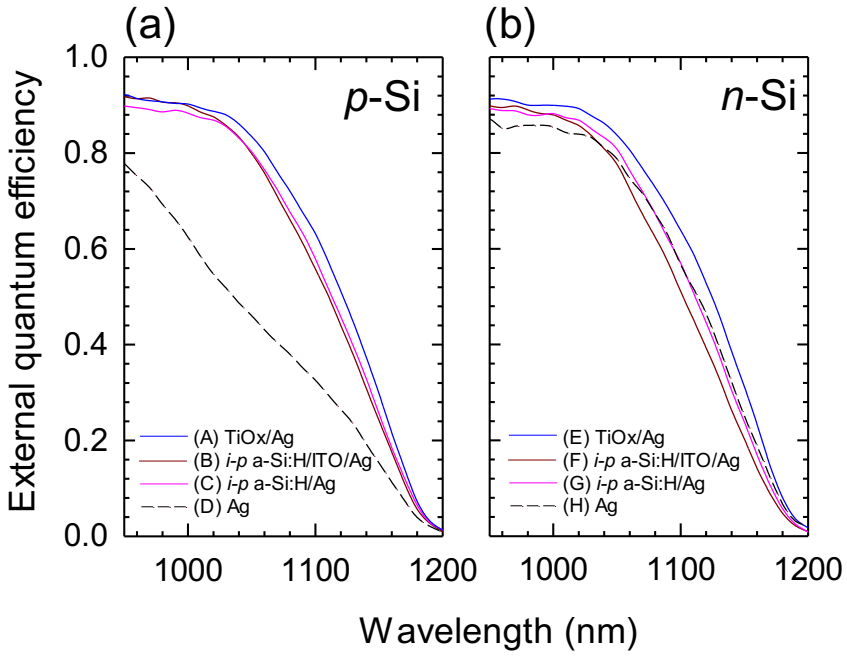

Figure 5. EQE spectra in the infrared wavelengths (900-1200 nm) of (a) *p*-Si and (b) *n*-Si solar cells with different hole contacts (blue: TiO_x/Ag, dark red: *i-p* a-Si:H/ITO/Ag, pink: *i-p* a-Si:H/Ag, black broken: Ag).

Overall, these results demonstrate that TiO_x functions as an efficient hole-selective passivating rear contact, as high performing as an *i-p* a-Si:H stack. Nevertheless, the efficiencies

attained in this work are still at around 20% which is primary limited by the lower J_{sc} (~38 mA cm^{-2}) compared with that of the conventional PERC cells (41-42 mA cm^{-2}) (2). The lower J_{sc} in our devices can be mainly attributed to the parasitic absorption loss caused by both the unoptimized *i*-*n* a-Si:H contact layers and the transparent conductive oxide (TCO) electrode at the front. A fine tuning of the thicknesses of *i*-*n* a-Si:H layers results in marginal gains in J_{sc} and efficiency (e.g., J_{sc}=38.8 mA cm^{-2}, efficiency=20.1% for *n*-Si). Thus, it is expected that much higher efficiency can be achieved by applying TiO_x/Ag bilayer to the PERC structure where neither a-Si:H nor TCO layer is used. Replacing the typical AlO_x/SiN_x/Al layers stack employed in PERC architecture with the TiO_x/metal bilayer offers several advantages: First, it is possible to eliminate Si-metal contact completely at the rear, which can essentially improve the rear surface passivation. Second, TiO_x/metal bilayer can be deposited entire area of the rear surface instead of the point contact design, which can reduce the process complexity. From an electrical point of view, an ideal one-dimensional hole transport is realized from Si absorber to the rear electrode through the TiO_x layer, instead of the two-dimensional transport towards the Si/metal point contact, which can decrease the electrical path length and thus the series resistance. Finally, the use of Ag and Cu rear electrode instead of Al increases the optical reflectivity at the rear, which can improve the infrared response.

Nevertheless, there still remain several challenges in industrial application of the TiO_x/metal bilayer. The use of Ag is not economically favourable and should be replaced with the cheaper metal. However, the minimum required thickness of Ag should be thinner than 50 nm and the metal layer can be thickened by depositing different metal such as Al over the Ag layer. Replacing the Ag by Cu is another option. Currently, however, we have seen that the use of Cu results in lower FF as shown in Figure 2(c). We found that post annealing after Cu sputtering decreases FF substantially. In fact, an initial efficiency of 19% was attained which is as high as

the case of Ag in the initial state (Supporting Information: Figure S3**)**. Although no notable difference is found in STEM and EDX analysis on TiO_x/Cu interface (Supporting Information: Figure S4**)** in comparison with that on TiO_x/Ag interface, it is speculated that some chemical reaction occurs at the TiO_x/Cu interface during the annealing. A similar annealing-induced FF degradation was observed in TiO_x/Ti contact for *n*-Si. The origin of these degradation phenomena remains unclear and needs further investigation. Another challenge is that the high temperature thermal budget would influence the passivation properties of the Si/TiO_x interface, as the process temperature used in this study (<300 °C) is much lower than that used in PERC solar cell production which generally involves high temperature firing process during metallization. Although this temperature issue has not been examined in this study so far, the new process flow in which a high-temperature process used for the front followed by low-temperature process for the rear would be a possible solution.

Finally, we address the possibility of the TiO_x for multijunction device applications. Replacing the capping metal with the TCO layers such as ITO provides the transparent hole-selective passivating contact. Fortunately, the WFs of these conductive metal oxide materials are as high as Ag. In fact, the solar cell featuring TiO_x/ITO front contact works with >21% efficiency (17). This offers the opportunity of combining the low-cost Si solar cells such as PERC with the perovskite solar cells via the transparent passivating contact between the top and bottom cells. The research is ongoing and will be presented in the near future.

3. Conclusions

We have demonstrated that the TiO_x/metal bilayer applied at the rear of Si solar cell performs as efficient hole-selective passivating contact as *i-p* a-Si:H layer stack. We found that the

high-WF (>4.6 eV) of the capping metal is one of the keys in attaining the carrier accumulation and inversion in the *p*- and *n*-Si absorbers, respectively, providing multiple functions including field-effective passivation, hole selectivity and optical reflector. This all-in-one function of the TiO_x allows full area rear passivating contact. The results obtained in this work offer the opportunity of replacing the conventional point contact design with dielectric interlayers (e.g., Al_2O_3/SiN_x) which is most widely used in the Si solar cell industries. The technique developed here would also enable the integration such commercial Si cell architecture into tandem solar cells.

4. Experimental Section

ALD and HPT processes for TiO_x layers:

TiO_x layers were deposited by an ALD system (FlexAL, Oxford Instruments) at a substrate heater temperature of 260 °C using titanium tetraisopropoxide (TTIP) and H_2O vapor as source gases (17). By repeating ALD cycle for 128 times, ~5 nm-thick TiO_x layer was deposited. The layer thickness was characterized by *in situ* spectroscopic ellipsometry (J.A. Woollam). Then, samples were subjected to an HPT by using a remote inductively-coupled plasma (17). To shorten the HPT time, a DC bias voltage (~30 V) was applied to the substrate by using another rf excitation source.

Solar cell fabrication:

In this study, *n*- and *p*-type crystalline Si wafers (float zone, 2-3 Ωcm, (100) orientation, 280 μm thick) were used. The front-texture and rear-planar structure was prepared by the following process step. Firstly, a SiN_x layer was deposited on the single side of the Si wafer by plasma-enhanced chemical vapor deposition (PECVD). This SiN_x served as a protection layer during the following etching process. Then, random pyramidal textures were formed on the uncoated front

side by wet-chemical etching in a KOH-based solution (Hayashi Pure Chemical, Pure Tech). The SiN_x layer was stripped by immersing the wafer in a diluted HF solution.

The single-side-textured wafers were cleaned in our standard cleaning processes (42). Undoped (*i*-type) and phosphorous-doped (*n*-type) a-Si:H layers were deposited on the front textured side of the Si wafers by PECVD (42). TiO_x layer was deposited by ALD on the rear planar side of the Si wafers. As a reference, a standard SHJ solar cell was prepared by depositing *i*-type and boron-doped (*p*-type) a-Si:H layers on the rear instead of TiO_x layer. After that, the rear surface was entirely metallized by magnetron sputtering or electron beam evaporation, which was described in detail in the main text. For textured side, ITO layers (~70 nm) were formed by a DC magnetron sputtering and then annealed at 180 °C under a low vacuum (17). Finally, Ag-grid electrodes were sputtered on top of the ITO layers.

***Characterization*:**

The τ_{eff} and iV_{oc} of solar cells before metallization were measured using a QSSPC setup (Sinton Instruments, WCT-120). After metallization, the J-V parameters of solar cells were measured at 25 °C under illumination (air mass 1.5 global, 100 mW cm^{-2}) using a dual-light source WACOM sun simulator. The illumination area (1.045 cm^2) was defined by using a black shading mask whose aperture area was slightly smaller than that of the electrode on the emitter side. EQE spectra were measured with a Bunkou-Keiki CEP-97 setup under a modulated monochromatic light illumination superimposed on a DC white bias light. As the illumination area of the EQE measurement is larger than the cell area, the black shading mask was used same as the J-V measurement. The PL measurement was carried out in an ITES PVX1000+POPLI-Λ system. The samples were homogeneously illuminated by an excitation laser with a wavelength of 850 nm

through a beam expander and a PL signal was recorded in a Si charge coupled device (CCD) camera with a cut-on wavelength of 990 nm. STEM and EDX measurements were performed at JFE streel Inc. Japan. Cross-sections of the samples were prepared by a focused ion beam milling technique and observed by STEM equipped with a HAADF detector combined with EDX spectroscopy at an acceleration voltage of 200 kV (JEOL JEM-ARM200F). To avoid the electron-beam induced degradation of the samples, the EDX scanning was done under the minimum irradiation condition. G-V measurements were carried out using a Keysight E4980A precision LCR Meter at a frequency of 1 kHz. The top contact was made by thermally evaporated Al or Au (~100 nm) through a metal mask. The back contact was created by evaporating a blanket Al layer directly onto the *n*-Si substrate using thermal evaporation. Kelvin Probe (KP) measurements were conducted in a Scanning KP020 instruments by KP Technologies, and were used to acquire the CPD of the samples without metallization and both in the dark, or under halogen lamp illumination with an intensity ~50 mW cm^{-2} at the sample's surface.

Supporting information

Capacitance-voltage measurements for various test frequencies for metal/*n*-Si/TiO_x/metal samples, and surface photovoltage CPD measurements of SiN_x and Al_2O_3 layers; CPD measurements at all stages of TiO_x processing; J-V parameters of *p*- and *n*-Si solar cells featuring a TiO_x/Cu rear contact; HAADF-STEM cross-sectional image and EDX analysis of a *p*-Si solar cell that has a TiO_x/Cu rear contact.

AUTHOR INFORMATION

Corresponding Author

*Takuya Matsui. E-mail: t-matsui@aist.go.jp

Author Contributions

T.M. designed the experiments, performed the ALD process and analysed the experimental data. H.S. performed PL measurements and established the baseline processes and characterization of SHJ solar cells in AIST. S.M. and R.S.B performed and analysed G-V and KP characterization. All authors discussed the results and commented on the manuscript.

Notes

The authors declare no competing financial interest.

ACKNOWLEDGMENT

We are grateful to T. Oku, Y. Sato, Y. Muto and M. Tanabe for the technical assistance in wafer preparation, cell fabrication and characterization. We particularly acknowledge to M. Yamazaki for assisting the ALD process and to T. Kaku for electron-beam evaporation which were conducted at the AIST Nano-Processing Facility, supported by “Nanotechnology Platform Program” of the Ministry of Education, Culture, Sports, Science and Technology (MEXT), Japan. This work has received funding from the New Energy and Industrial Technology Development Organization (NEDO), Japan. R.S.B was supported by the Royal Academy of Engineering under the Research Fellowship scheme. This work was supported by the UK Engineering and Physical Sciences Research Council grant number EP/V038605/1, and by the John Fell Fund at Oxford University.

REFERENCES

(1) International Technology Roadmap for Photovoltaic (ITRPV), 2021 Results, 13th edition. https://www.vdma.org/international-technology-roadmap-photovoltaic (accessed: September 2022).

(2) Green, M. A.; Blakers, A. W.; Zhao, J.; Milne, A. M.; Wang, A.; Dai, X. Characterization of 23-percent efficient silicon solar cells. *IEEE Trans. Electron Dev.* **1990**, 37, 331–336.

(3) Dullweber, T.; Schmidt, J. Industrial Silicon Solar Cells Applying the Passivated Emitter and Rear Cell (PERC) Concept—A Review. *IEEE J. Photovolt.* **2016**, 6, 1366−1381.

(4) Allen, T. G.; Bullock, J.; Yang, X.; Javey, A.; De Wolf, S. Passivating Contacts for Crystalline Silicon Solar Cells. *Nat. Energy* **2019**, 4, 914−928.

(5) Taguchi, M.; Yano, A.; Tohoda, S.; Matsuyama, K.; Nakamura, Y.; Nishiwaki, T.; Fujita, K.; Maruyama, E. 24.7% Record Efficiency HIT Solar Cell on Thin Silicon Wafer. *IEEE J. Photovolt.* **2014**, 4, 96−99.

(6) Yoshikawa, K.; Kawasaki, H.; Yoshida, W.; Irie, T.; Konishi, K.; Nakano, K.; Uto, T.; Adachi, D.; Kanematsu, M.; Uzu, H.; Yamamoto, K. Silicon Heterojunction Solar Cell with Interdigitated Back Contacts for a Photoconversion Efficiency over 26%. *Nat. Energy* **2017**, 2, 17032.

(7) Long, W.; Yin, S.; Peng, F.; Yang, M.; Fang, L.; Ru, X.; Qu, M.; Lin, H.; Xu, X. On the limiting efficiency for silicon heterojunction solar cells. *Sol. Energy Mater. Sol. Cells*, **2021**, 231, 111291.

(8) Richter, A.; Müller, R.; Benick, J.; Feldmann, F.; Steinhauser, B; Reichel, C.; Fell, A.; Bivour, M.; Hermle, M.; Glunz, S. W. Design rules for high-efficiency both-sides-contacted silicon solar cells with balanced charge carrier transport and recombination losses. *Nat. Energy* **2021**, 6, 429–438.

(9) Haase, F.; Hollemann, C.; Schäfer, S.; Merkle, A.; Rienäcker, M.; Krügener, J.; Brendel, R.; Peibst, R. Laser Contact Openings for Local Poly-Si-Metal Contacts Enabling 26.1%-Efficient POLO-IBC Solar Cells. *Sol. Energy Mater. Sol. Cells* **2018**, 186, 184−193.

(10) Battaglia, C.; Yin, X.; Zheng, M.; Sharp, I. D.; Chen, T.; McDonnell, S.; Azcatl, A.; Carraro, C.; Ma, B.; Maboudian, R.; Wallace, R. M.; Javey, A. Hole Selective MoO_x Contact for Silicon Solar Cells. *Nano Lett*. **2014**, 14, 967−971.

(11) Bivour, M.; Temmler, J.; Steinkemper, H.; Hermle, M. Molybdenum and Tungsten Oxide:High Work Function Wide Band Gap Contact Materials for Hole Selective Contacts of Silicon Solar Cells. *Sol. Energy Mater. Sol. Cells* **2015**, 142, 34−41.

(12) Liu, Z.; Lin, W.; Chen, Z.; Chen, D.; Chen, Y.; Shen, H.; Liang, Z. Enhanced Hole Extraction of WO_x/V_2O_x Dopant-Free Contact for p-type Silicon Solar Cell. *Adv. Mater. Interfaces* **2022**, 4, 2102374.

(13) Gerling, L. G.; Mahato, S.; Morales-Vilches, A.; Masmitja, G.; Ortega, P.; Voz, C.; Alcubilla, R.; Puigdollers, J. Transition Metal Oxides as Hole-Selective Contacts in Silicon Heterojunctions Solar Cells. *Sol. Energy Mater. Sol. Cells* **2016**, 145, 109−115.

(14) Halbich, M. U.; Zielke, D.; Gogolin, R.; Rüdiger, S. S.; Wilfried, L.; Schmidt, J. Improved surface passivation and reduced parasitic absorption in PEDOT:PSS/c-Si heterojunction solar cells through the admixture of sorbitol. *Sci. Rep.* **2019**, 9, 9775.

(15) Dréon, J.; Jeangros, Q.; Cattin, J.; Haschke, J.; Antognini, L.; Ballif, C.; Boccard, M. 23.5%-Efficient Silicon Heterojunction Silicon Solar Cell Using Molybdenum Oxide as Hole-Selective Contact. *Nano Energy*, **2020**, 70, 104495.

(16) Matsui, T.; Bivour, M.; Ndione, P. F.; Bonilla, R. S.; Hermle, M. Origin of the Tunable Carrier Selectivity of Atomic-Layer-Deposited TiO_x Nanolayers in Crystalline Silicon Solar Cells. *Sol. Energy Mater. Sol. Cells* **2020**, 209, 110461.

(17) Matsui, T.; Bivour, M.; Hermle, M.; Sai, H. Atomic-layer-deposited TiO_x nanolayers function as efficient hole-selective passivating contacts in silicon solar cells. *ACS Appl. Mater. Interfaces* **2020**, 12, 49777−49785.

(18) Yang, X.; Bi, Q.; Ali, H.; Davis, K.; Schoenfeld, W. V.; Weber, K. High-Performance TiO_2-Based Electron-Selective Contacts for Crystalline Silicon Solar Cells. *Adv. Mater*. **2016**, 28, 5891−5897.

(19) Bullock, J.; Wan, Y.; Hettick, M.; Zhaoran, X.; Pheng, S.; Yan, D.; Wang, H.; Ji, W.; Samundsett, C.; Hameiri, Z.; Macdonald, D.; Cuevas, A.; Javey, A. Dopant-Free Partial Rear Contacts Enabling 23% Silicon Solar Cells. *Adv. Energy Mater*. **2019**, 9, 180336.

(20) Yin, X.; Battaglia, C.; Lin, Y.; Chen, K.; Hettick, M.; Zheng, M.; Chen, C.-Y.; Kiriya, D.; Javey, A. 19.2% Efficient InP Heterojunction Solar Cell with Electron-Selective TiO_2 contact. *ACS Photonics* **2014**, 1, 1245−1250.

(21) Burschka, J.; Pellet, N.; Moon, S.-J.; Humphry-Baker, R.; Gao, P.; Nazeeruddin, M. K.; Gratzel, M. Sequential Deposition as a Route to High-Performance Perovskite-Sensitized Solar Cells. *Nature* **2013**, 499, 316−319.

(22) Lee, M.; Teuscher, J.; Miyasaka, T.; Murakami, T. N.; Snaith, H. J. Efficient Hybrid Solar Cells Based on Meso-Superstructured Organometal Halide Perovskites. *Science* **2013**, 338, 643−647.

(23) Aisa, D.; Anzivino, G.; Barbanera, M.; Bizzarri, M.; Bizzeti, A.; Bucci, F.; Campeggi, C.; Carassiti, V.; Cassese, A.; Cenci, P.; Ciaranfi, R.; David, C.; Duk, V.; Iacopini, E.; Imbergamo, E.; Latino, G.; Lenti, M.; Lollini, R.; Malett F.; Pepe, M.; Piccini, M.; Piluso, A.; Schneider, T.; Scolieri, G.; Van Stenis, M.; Volpec, R. Mirror system of the RICH detector of the NA62 experiment. JINST **2017**, 12, P12017.

(24) Hermle, M.; Feldmann, F.; Bivour, M.; Goldschmidt, J. C.; Glunz, S. W. Passivating contacts and tandem concepts: Approaches for the highest silicon-based solar cell efficiencies. *Appl. Phys. Rev*. **2020**, 7, 021305.

(25) Michaelson, H. B. The work function of the elements and its periodicity. *J. Appl. Phys.* **1977**, 48, 4729−4733.

(26) Dweydari, A. W.; Mee, C. H. B. Work function measurements on (100) and (110) surfaces of silver. *Phys. Status solidi (a)* **1975***,* 27, 223−230.

(27) Derry, G. N.; Kern, M. E.; Worth, E. H. Recommended values of clean metal surface work functions. *J. Vac. Sci. Technol. A* **2015**, 33, 060801.

(28) Dweydari, A. W.; Mee, C. H. B. Oxygen adsorption on the (111) face of silver. *Phys. Status Solidi (a)* **1973**, 17, 247−250.

(29) Magari, Y.; Makino, H.; Hashimoto, S.; Furuta, M. Origin of work function engineering of silver oxide for an In–Ga–Zn–O Schottky diode. *Appl. Surf. Sci*., **512**, 2020, 144519.

(30) Winch, R. P. The Photoelectric Properties of silver. *Phys. Rev*. **1931**, 37, 1269−1275.

(31) Sinton, R. A.; Cuevas, A. Contactless determination of current–voltage characteristics and minority-carrier lifetimes in semiconductors from quasi-steady-state photoconductance data. *Appl. Phys. Lett*., **1996**, 69, 2510.

(32) Nicollian, E. H.; Goetzberger, A. MOS conductance technique for measuring surface state parameters. *Appl. Phys. Lett.* **1965**, 7, 216−219.

(33) Bonilla, R. S.; Al-Dhahir, I.; Yu, M.; Hamer, P.; Altermatt, P. P. Charge fluctuations at the Si–SiO_2 interface and its effect on surface recombination in solar cells. *Sol. Energy Mater. Sol. Cells*. **2020**, 215, 110649.

(34) Yu, M.; McNab, S.; Al-Dhahir, I.; Patrick, C. E.; Altermatt, P. P.; Bonilla, R. S. Extracting band-tail interface state densities from measurements and modelling of space charge layer resistance. *Sol. Energy Mater. Sol. Cells* **2021**, 231, 111307.

(35) Bonilla, R. S.; Reichel, C.; Hermle, M.; Wilshaw, P. R. On the location and stability of charge in SiO_2/SiN_x dielectric double layers used for silicon surface passivation. *J. Appl. Phys*. **2014**, 115, 144105.

(36) Bonilla, R. S. Modelling of Kelvin Probe Surface Voltage and Photovoltage in Dielectric-Semiconductor Interfaces. *Mater. Res. Express*, **2022**, 9, 085901.

(37) Pain, S. L.; Grant, N. E.; Murphy, J. D. Room Temperature Enhancement of Electronic Materials by Superacid Analogues. *ACS Nano* **2022**, 16, 1260−1270.

(38) Bonilla, R. S. Jennison, N.; Clayton-Warwick, D.; Collett, K. A.; Rands, L.; Wilshaw, P. R. Corona Charge in SiO_2: Kinetics and Surface Passivation for High Efficiency Silicon Solar Cells. *Energy Procedia*, **2016**, 92, 326−335.

(39) Schroder, D. K. Surface voltage and surface photovoltage: history, theory and application. *Meas. Sci. Technol*. **2001**, 12, R16.

(40) Baikie, I. D. Surface Potential and Surface Photovoltage of Oxide and Nitride coated multicrystalline Silicon Solar Cells using a Scanning Kelvin Probe. *MRS Online Proceedings Library*, **2003**, 808, 467–472.

(41) Li, S.; Pomaska, M.; Lambertz, A.; Duan, W.; Bittkau, K.; Qiu, D.; Yao, Z.; Luysberg, M.; Steuter, P.; Köhler, M.; Qiu, K.; Hong, R.; Shen, H.; Finger, F.; Kirchartz, T.; Rau, U.; Ding, K. Transparent-conductive-oxide-free front contacts for high-efficiency silicon heterojunction solar cells. *Joule*, **2021**, 5, 1535−1547.

(42) Sai, H.; Oku, T.; Sato, Y.; Tanabe, M.; Matsui T.; Matsubara, K. Potential of Very Thin and High-Efficiency Silicon Heterojunction Solar Cells. *Prog. Photovolt. Res. Appl.* **2019**, 27, 1061−1070.

For Table of Contents Only